Dalton Transactions

RSC Publishing

PAPER

View Article Online
View Journal | View Issue

Cite this: *Dalton Trans.*, 2013, **42**, 9565

Multifunctional nanocomposites of lanthanide (Eu^{3+}, Tb^{3+}) complexes functionalized magnetic mesoporous silica nanospheres covalently bonded with polymer modified ZnO†

Bing Yan* and Yan-Fei Shao

Received 17th January 2013,
Accepted 10th April 2013

DOI: 10.1039/c3dt50169h

www.rsc.org/dalton

Methacrylic-group-modified ZnO nanoparticles (designated ZnO-MAA) prepared through the sol–gel process are copolymerized with 2-hydroxyethyl methacrylate (HEMA) to form ZnO-MAA-PHEMA hybrid system. ZnO-MAA-PHEMA unit is functionalized with 3-(triethoxysilyl)-propyl isocyanate (TEPIC) to form ZnO-MAA-PHEMA-Si hybrids, and then is incorporated with oleic acid-modified Fe_3O_4 nanoparticles by co-condensation of tetraethoxysilane (TEOS) and ZnO-MAA-PHEMA-Si. Subsequently, ZnO-polymer covalently bonded mesoporous silica nanospheres are assembled using cetyltrimethylammonium bromide (CTAB) surfactant as template. Furthermore, lanthanide (Eu^{3+}, Tb^{3+}) complexes with nicotinic acid (NTA), isonicotinic acid (INTA) and 2-chloronicotinic (CNTA) are introduced by coordination bonds, resulting in the final multifunctional nanocomposites. The detailed physical characterization of these hybrids is discussed in detail. It reveals that they possess both magnetic and luminescent properties. Especially $Eu(ZnO\text{-}MMS)(CNTA)_3$ and $Tb(ZnO\text{-}MMS)(NTA)_3$ present high quantum yield values of 32.2% and 68.5%, respectively. The results will lay the foundation for further application in biomedical and biopharmaceutical fields.

Introduction

It is generally known that lanthanide complexes possess many advantages in luminescent materials. Such excellent traits such as narrow-width, intense emission bands, high quantum efficiency, high color purity and long lifetimes have made them very attractive for many years.[1] Multifunctional hybrids or nanocomposites based on luminescent lanthanide complexes have seen a great interest in recent years both in fundamental research and practical application, in which the thermal stability and mechanical property of lanthanide complexes can be improved.[2] Typically, lanthanide complexes can be introduced into an organic polymers,[3] liquid crystals[4] or inorganic matrices (silica-based material, microporous and mesoporous host, nanocomposite and other inorganic oxide network).[5] For simple organic polymer host, the exciting application is counteracted by softness, hydrophilic nature of polymer and sensitivity to external environment such as pH, temperature and so on. Therefore, the further composition of polymer and inorganic matrix has been investigated extensively. While the non-crystalline nature of these hybrid materials makes them difficult to determine the exact composition and structures. So, the research focus has shifted to the introduction of crystalline building blocks into hybrid systems to combine inorganic–organic hybrids and nanocomposites.[2] Besides, the multi-component assembly of hybrid systems with different components may realize the functional integration to be favorable for practical applications.

As is well known, II–VI group semiconductor nanoparticles, so-called quantum dots (QDs), possess unique optical properties and promising applications.[6] Their strong bandgap luminescence makes them have a lot of potential value for luminescent biolabeling.[7] However, most particles prepared are luminescent only in nonpolar environment, restricting the application in the fields of biology. In addition, these nanoparticles are inclined to agglomerate and some of them are instable when exposed to water, air and sunlight.[8] During the past few years, many efforts have been widely carried out to solve these problems.[9,10] Among the methods, isolation with polymer shell may be the best choice. Then, as discussed earlier, we can introduce polymer unit to inorganic host like silica microspheres because of the polymer' disadvantages.

Department of Chemistry, Tongji University, State Key Lab of Water Pollution and Resource Reuse, Tongji University, Siping Road 1239, Shanghai, 200092, P. R. China. E-mail: byan@tongji.edu.cn; Fax: +86-21-65981097; Tel: +86-21-65984663

†Electronic supplementary information (ESI) available. See DOI: 10.1039/c3dt50169h

Here, the luminescence of ZnO QDs might not be the best among the nanoparticles, but ZnO is a kind of non-poisonous, cheap and chemically stable material, this makes it more popular. Meanwhile, the luminescence of lanthanide complexes may be promoted by connecting II–VI group semiconductor nanoparticles.[11]

On the other hand, superparamagnetic organic/inorganic hybrids have been investigated massively ever since Ugelstad prepared superparamagnetic polystyrene microspheres for immunity separation.[12] Magnetic nanoparticles, especially Fe_3O_4 nanoparticles with unique magnetic response and low cytotoxicity, have been widely used in different fields. Their applications cover environmental and nanobiotechnological areas like biosensor, targeted drug delivery, imaging, and so on.[13] But it may suffer from fast biodegradation while being exposed to biological environments directly due to its relatively small sizes. The issues can be addressed through core–shell structures such as coating the Fe_3O_4 nanoparticles surface with a silica layer.[14] The surface silanol groups easily react with different compounds to obtain functional units and thus it is convenient to link other components such as luminescent materials.

In this paper, we try to assemble multifunctional systems including magnetic unit (oleic acid-modified Fe_3O_4 nanoparticles by co-condensation of tetraethoxysilane (TEOS)) and luminescent components (ZnO-MAA-PHEMA-Si and Eu^{3+}/Tb^{3+} complexes), whose integration of magnetic and luminescent properties of different components into a single nanocomposite system might greatly extend their applications in biomedical and biopharmaceutical fields. Detailed characterizations of the multifunctional materials are discussed.

Experimental section

Materials

Lanthanide nitrates ($Ln(NO_3)_3{\cdot}6H_2O$, Ln = Eu, Tb) were obtained by dissolving their oxides (Eu_2O_3, Tb_4O_7) in concentrated nitric acid. Tetraethoxysilane (TEOS), 3-(triethoxysilyl)-propyl isocyanate (TEPIC), methacrylic acid (MAA) and lithium hydroxide monohydrate ($LiOH{\cdot}H_2O$) were purchased from Shanghai YaoHua chemical plant. Ferric chloride ($FeCl_3{\cdot}6H_2O$), ferrous chloride ($FeCl_2{\cdot}4H_2O$), ammonia solution ($NH_3{\cdot}H_2O$, 25–28%), oleic acid (90%) and cetyltrimethylammonium bromide (CTAB) were purchased from Aldrich and used as received. The solvent chloroform ($CHCl_3$) was used after desiccation with anhydrous magnesium sulfate. All the other reagents were analytically pure.

Preparation of Fe_3O_4 nanoparticles

Oleic acid-modified Fe_3O_4 nanoparticles were prepared in the light of the co-precipitation of ferrous and ferric ion solutions with 1 : 2 molar ratio.[13b,16] $FeCl_3{\cdot}6H_2O$ (2 mmol, 0.541 g) and $FeCl_2{\cdot}4H_2O$ (1 mmol, 0.199 g) were dissolved in deionized water (30 mL) under argon atmosphere with vigorous stirring at 80 °C. Then 3 mL ammonium hydroxide was added into the solution under rapid stirring. After 30 min, 0.1 g oleic acid was added to the mixture solution. The black suspension was continuously stirred for about 2 h at 80 °C. Then the black solid product was precipitated and washed with deionized water.

Preparation of ZnO-MAA-PHEMA-Si nanoparticles

Methacrylic-group-modified ZnO nanoparticle (designated ZnO-MAA) was obtained by the reaction between $[H_2C{=}C(CH_3)CO_2]_2Zn$ and LiOH ethanol solution with the molar ratio [LiOH]/[Zn] = 3.5.[17] The freshly dried ZnO-MAA solid (1 mmol) was added in ethanol solution containing 2-hydroxyethyl methacrylate (1 mL), then the initiator benzoyl peroxide (BPO, 0.005 g) was added into the solution. The mixture was agitated magnetically at 60 °C for about 6 h under an argon atmosphere purging. The products were centrifuged and purified to obtain ZnO-MAA-PHEMA nanoparticles. Afterwards, the as-prepared ZnO-MAA-PHEMA nanoparticles were dissolved in the solvent of anhydrous tetrahydrofuran (THF, 20 mL), then 2 mmol of NaH (0.048 g) was added. The mixture was agitated magnetically and thermal treatment was performed at 60 °C. After 2 h, TEPIC (2.0 mmol, 0.495 g) was added dropwise into the refluxing solution. The mixture was heated at 65 °C for approximately 12 h in an argon atmosphere. A viscous liquid product was obtained after isolation and purification.

Preparation of magnetic mesoporous silica nanospheres covalently bonded with polymer modified ZnO (denoted as ZnO-MMS)

ZnO-MMS hybrids were prepared according to the literature.[18] Oleic acid-modified Fe_3O_4 nanoparticles (15 mg) were dispersed in $CHCl_3$ (2 mL) by sonication, then the mixture was added to aqueous solution (10 mL) containing 0.1 g CTAB. Through stirring vigorously, a homogeneous oil-in-water microemulsion was obtained. For evaporating the $CHCl_3$, the resulting solution was heated at 65 °C for about 30 min, producing a black Fe_3O_4–CTAB solution. CTAB (0.05 g) and NaOH (1.4 mL, 1 M) were dissolved in 38 mL deionized water with stirring at room temperature. Then Fe_3O_4–CTAB solution (10 mL) prepared above were added to the system, which was heated to 80 °C. While being stirred vigorously, 0.4 mL TEOS and 0.02 g ZnO-MAA-PHEMA-Si synthesized above were added to the solution. The reaction solution was maintained at 80 °C for about 2 h with agitating vigorously. The resulting product was centrifuged and washed with deionized water. After further being dried at room temperature, surfactant CTAB was removed by Soxhlet extraction with ethanol under reflux for 2 days.

Preparation of lanthanide complexes functionalized magnetic mesoporous silica nanospheres covalently bonded with polymer modified ZnO (denoted as $Ln(ZnO\text{-}MMS)(L)_3$, Ln = Eu, Tb, L = NTA, INTA; $Eu(ZnO\text{-}MMS)(CNTA)_3$)

The precursor ZnO-MMS and assistant ligands (nicotinic acid (NTA), isonicotinic acid (INTA) and 2-chloronicotinic (CNTA)) (NTA, INTA and CNTA for Eu, NTA and INTA for Tb) were dissolved in DMF solvent, then adding $Ln(NO_3)_3{\cdot}xH_2O$ ethanol

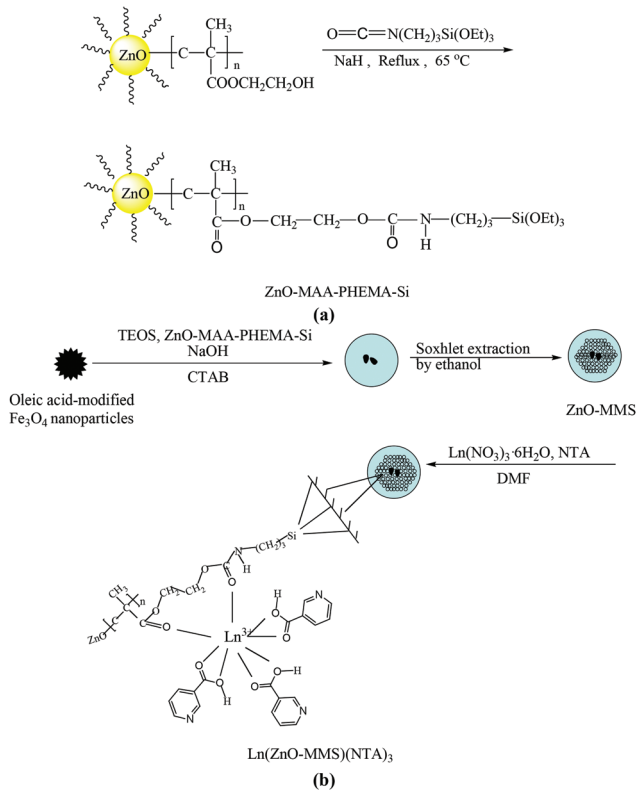

Fig. 1 Selected scheme of the synthesis process of ZnO-MAA-PHEMA-Si (a) and the predicted composition of Ln(ZnO-MMS)$(NTA)_3$ (b).

solution with the molar ratio Ln^{3+} : ZnO-MMS : NTA/INTA/CNTA = 1 : 1: 3. The mixture was stirred for 12 h at room temperature. The resulting product was centrifuged and washed with EtOH. After being dried under vacuum at 60 °C, the end product was obtained as shown in Fig. 1. The contents of Ln^{3+} ions (Eu^{3+}, Tb^{3+}) and Zn^{2+} in the hybrids were determined with ICP-OES and N were determined with elemental analysis. For Eu-(ZnO-MMS)$(NTA)_3$ (wt. %): Eu 4.8, Zn 4.05, Fe 5.53, N 1.30; for Eu(ZnO-MMS)$(INTA)_3$ (wt. %): Eu 4.7, Zn 3.99, Fe 5.50, N 1.29; for Eu(ZnO-MMS)$(CNTA)_3$ (wt. %): Eu 4.65, Zn 3.91, Fe 5.50, N 1.25; for Tb(ZnO-MMS)$(NTA)_3$ (wt. %): Tb 4.25, Zn 3.53, Fe 4.15, N 1.25; for Tb(ZnO-MMS)$(INTA)_3$ (wt. %): Tb 4.20, Zn 3.65, Fe 4.08, N 1.25. According to the content of Ln^{3+}, Zn^{2+} and N, it was predicted that the molar ratio of Ln : Zn : N is close to 1 : 2 : 3.

Physical measurements

The elemental analyses (N) of the ternary lanthanide hybrids were measured with a CARIO-ERBA 1106 elemental analyzer and the contents of metal element (Ln, Zn, Fe) were determined on the Perkin Optima 2100DV Inductively Coupled Plasma Optical Emission Spectrometer (ICP-OES). Fourier transform infrared (FTIR) spectra were measured within the 4000–400 cm^{-1} region on a Nexus 912 AO446 spectrophotometer with the KBr pellet technique. Magnetic measurements were performed using a LakeShore 7307 vibration sample magnetometer (VSM). The X-ray powder diffraction patterns (XRD) were recorded on a Bruker D8 diffractometer (40 mA–40 kV) using monochromated Cu Kα1 radiation (k = 1.54 Å) over the 2θ range of 10–70° and 0.6–6°, respectively. Scanning electronic microscope (SEM) images were obtained with a Philps XL-30. Transmission electron microscope (TEM) experiments were conducted on a JEOL2011 microscope operated at 200 kV or on a JEM-4000EX microscope operated at 400 kV. Luminescence (excitation and emission) spectra and luminescence lifetime measurements were carried out on an Edinburgh FLS920 phosphorimeter using a 450 W xenon lamp as the excitation source. The outer luminescent quantum efficiency was determined using an integrating sphere (150 mm diameter, $BaSO_4$ coating) from Edinburgh FLS920 phosphorimeter. The spectra were corrected for variations in the output of the excitation source and for variations in the detector response. The quantum yield can be defined as the integrated intensity of the luminescence signal divided by the integrated intensity of the absorption signal. The absorption intensity was calculated by subtracting the integrated intensity of the light source with the sample in the integrating sphere from the integrated intensity of the light source with a blank sample in the integrating sphere. All above measurements were completed under room temperature. Nitrogen adsorption–desorption isotherms were measured by a Nova 1000 analyzer at the liquid nitrogen temperature. Surface areas were calculated by the Brunauer–Emmett–Teller (BET) method and pore size distributions were evaluated from the desorption branches of the nitrogen isotherms using the Barrett–Joyner–Halenda (BJH) model. The ultraviolet-visible diffuse reflectance spectra were acquired by a BWS003 spectrophotometer.

Results and discussion

Fig. 1 shows the scheme for the composition and synthesis process of multi-component hybrid systems. MAA modified ZnO colloids are *in situ* formed after sol–gel process and then are composed with monomer HEMA through copolymerization reaction between the MAA unit and HEMA. So polyesters are indirectly connected with ZnO by covalent bonds with MAA unit as bridge.[17] Further, organically modified siloxane units are introduced through the reaction between the hydroxyl groups of HEMA unit and the inter ester group of TEPIC to form covalent linking system ZnO-MAA-PHEMA-Si.[15,18] Magnetic mesoporous silica nanospheres containing oleic acid-modified Fe_3O_4 nanoparticles can be assembled with above ZnO polymer composites through sol–gel reaction. On the other hand, europium and terbium nitrates and pyridine carboxylates (NTA, INTA, CNTA) ligands are *in situ* introduced to obtain the final multi-component hybrid systems through chemical bonds. Ln^{3+} (Ln = Eu, Tb) ions are coordinated to six oxygen atoms of three carboxylate molecules and two oxygen atoms of MAA-PHEMA-Si unit. Here the molar ratio of 1 : 2 : 3 of Ln : Zn : N verifies the basic composition and coordination environment around Ln^{3+} in the hybrid system.

The FT-IR spectrum data of ZnO-MMS and Eu(ZnO-MMS)$(L)_3$ (L = CNTA, NTA and INTA) hybrids are shown in Fig. 2. In

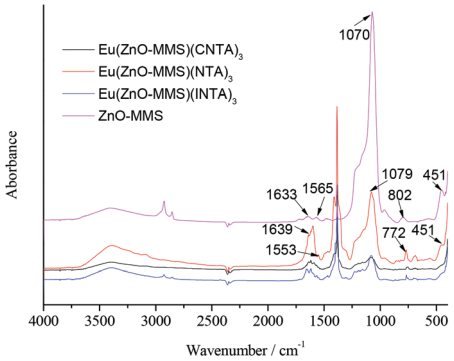

Fig. 2 FTIR spectra of ZnO-MMS and Eu(ZnO-MMS)$(L)_3$ (L = CNTA, NTA and INTA).

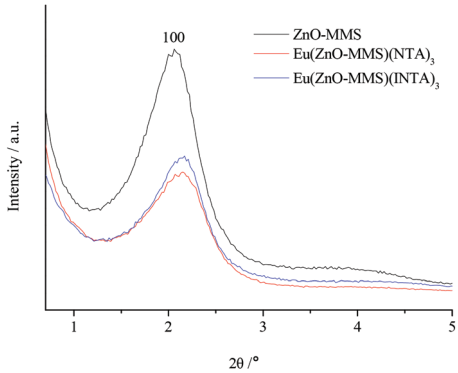

Fig. 3 Small-angle X-ray diffraction pattern of ZnO-MMS, Eu(ZnO-MMS)$(NTA)_3$ and Eu(ZnO-MMS)$(INTA)_3$.

ZnO-MMS host material, the obvious band appearing at 1070 cm^{-1} is due to the asymmetric Si–O stretching vibration modes, and the band at 802 cm^{-1} can be attributed to the symmetric Si–O stretching vibration. Besides, the band at 451 cm^{-1} is associated with the Si–O–Si bending vibration and the silanol (Si–OH) stretching vibration of surface groups is observed at 968 cm^{-1} [19] Comparing with ZnO-MMS, Eu(ZnO-MMS)$(L)_3$ hybrids exhibit the similar infrared absorption bands as the silica framework. The bands at 1633 and 1565 cm^{-1}, originating from the –CONH– group of ZnO-MAA-PHEMA-Si, can be observed both in ZnO-MMS and Eu(ZnO-MMS)$(L)_3$ hybrids, which indicates that ZnO-MAA-PHEMA group remains intact after the hydrolysis-condensation reaction and coordination reaction.

The selected ultraviolet-visible diffuse reflection spectra of the hybrid materials are given in Fig. S1† for Tb(ZnO-MMS)$(NTA)_3$ and Tb(ZnO-MMS)$(INTA)_3$, respectively. Both of them exhibit the similar broad absorption band in the UV-vis range (200–600 nm), which can be ascribed to the absorption of ligands NTA and INTA. In line with Dexter's exchange energy transfer theory,[20] it can be primarily forecast that the energy level difference between NTA and Tb^{3+} is appropriate so that the organic ligand can absorb adequate energy in ultra-visible region and then transfer it to Tb^{3+} within the hybrid materials. So the final materials can be supposed to have splendid luminescence properties when the intramolecular energy transfer process has been accomplished. This is indeed proved by the emission spectra. Meanwhile, an inverse absorption peak located at about 545 nm can be observed clearly, which is attributed to the characteristic emission of Tb^{3+} after being excited by the UV component in the incident ray during the measurement and the position of the characteristic emission lines is the same as that of Tb^{3+} ions. These inverse peaks are a result of the self-absorption of the materials. When compared with each other of the two spectra, it can be found that the two broad absorption bands are identical, illustrating the energy transfer system between the two organic ligands and Tb^{3+} ions are similar.

Fig. S2† is the selected wide-angle X-ray diffraction pattern of MMS and ZnO-MMS, exhibiting that the obtained hybrid materials are amorphous from 10° to 70°. The two materials exhibit similar XRD patterns, with a broad peak centered on about 22.25°, which can be attributed to the amorphous inorganic silica backbone of the Si–O network. For MMS, the most characteristic diffraction peak of Fe_3O_4 nanoparticles appears at 35.50° and other peaks are mostly in line with the JCPDS file of Fe_3O_4 (JCPDS 01-1111, space group *Fd3m*). Compared with MMS, the most typical peak in the XRD pattern of ZnO-MMS appears at 35.72°, which not only has a slight shift but also is relatively low. This phenomenon may be due to the influence of ZnO unit, whose typical peak appears at 36.18°. Meanwhile, the relatively small peaks behind also exhibit a little difference when comparing ZnO-MMS to MMS.

Fig. 3 is the small-angle XRD pattern of ZnO-MMS, Eu(ZnO-MMS)$(NTA)_3$ and Eu(ZnO-MMS)$(INTA)_3$. It can be seen that all the samples exhibit an obvious diffraction band at the 2θ of 2°, which is indexed as the (100) diffraction and characteristic of MCM-41-type two-dimensional hexagonal (*P6mm*).[21] The d_{100} spacing values of the Eu(ZnO-MMS)$(NTA)_3$ and Eu(ZnO-MMS)$(NTA)_3$ are all 4.13 nm. They are almost the same as the SAXRD pattern of ZnO-MMS material (4.29 nm), demonstrating that the framework hexagonal ordering has been preserved well when the lanthanide ions are introduced. Furthermore, it can be observed that the diffraction intensity of the lanthanide complex functionalized materials have a decrease in comparison with the parent ZnO-MMS material, which may be due to the steric constraints of lanthanide complex onto the mesoporous framework of ZnO-MMS, resulting in a larger heterogeneity of the pores.

To further investigate the channel structure of these materials, the characterization of the nitrogen adsorption–desorption is carried out. Fig. 4 shows the selected isotherms for ZnO-MMS and Eu(ZnO-MMS)$(NTA)_3$ materials. According to IUPAC classification, the samples all display typical type IV isotherm with an H1 type hysteresis loop at high relative pressure, characteristic of highly ordered mesoporous materials with uniform size distributions.[22] It can be clearly observed that the volume of nitrogen adsorbed decreased with functionalization with lanthanide complex, which is indicative of a reduction in pore size. The textural data of the materials, such as BET

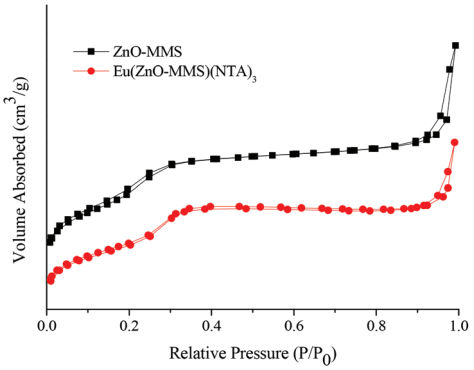

Fig. 4 N_2 adsorption–desorption isotherms of ZnO-MMS and Eu(ZnO-MMS)$(NTA)_3$.

Table 1 Structural parameters of ZnO-MMS and Eu(ZnO-MMS)$(NTA)_3$[a]

Sample	d_{100} (nm)	a_0 (nm)	S_{BET} ($m^2\ g^{-1}$)	V ($cm^3\ g^{-1}$)	D (nm)	t (nm)
ZnO-MMS	4.29	4.95	756	0.85	4.48	0.47
Eu(ZnO-MMS)$(NTA)_3$	4.13	4.77	551	0.57	4.16	0.61

[a] d_{100} is the $d(100)$ spacing, a_0 the cell parameter ($a_0 = 2\ d_{100}/\sqrt{3}$), S_{BET} the BET surface area, V the total pore volume, D_{BJH} the average pore diameter, and t the wall thickness, calculated by $a_0 - D$.

surface area (S_{BET}), total pore volume and BJH average pore diameter, are given in Table 1. It is known from Table 1, the material of ZnO-MMS possesses high S_{BET} of 756 $m^2\ g^{-1}$, a pore volume of 0.85 $cm^3\ g^{-1}$ and a BJH pore diameter of 4.48 nm, indicating its potential application as a host in luminescent materials. Compared with ZnO-MMS, the end product Eu(ZnO-MMS)$(NTA)_3$ shows a smaller surface area, pore size and pore volume, which may be due to the introduction of lanthanide complex to the channels of mesoporous materials ZnO-MMS leading to the ordered mesoporous structure decrease.

Fig. 5a and b presents the SEM images of as-synthesized MMS, and Eu(ZnO-MMS)$(NTA)_3$, respectively, both of which possesses the similar uniform and monodisperse nanosphere with about 200 nm sphere size. Fig. 5c–h shows transmission electron microscopy (TEM) images of Eu(ZnO-MMS)$(NTA)_3$ with different magnifications. The core–shell structure of end products can be seen clearly and the nanospheres are rather uniform and monodisperse, although most silica shells have captured more than one magnetic core. This is because the aggregation of Fe_3O_4 nanoparticles occur antecedent to or during co-condensation of TEOS and modified polymer ligand (ZnO-MAA-PHEMA-Si). The thickness of the silica shell can also be adjusted through changing the original amount of TEOS. The Fe_3O_4 nanoparticles prepared have a core diameter of about 10 nm, which is roughly estimated from the broadening of the peaks by using the Scherrer's equation (the XRD pattern in Fig. S3 in ESI†) and the black core in TEM images.

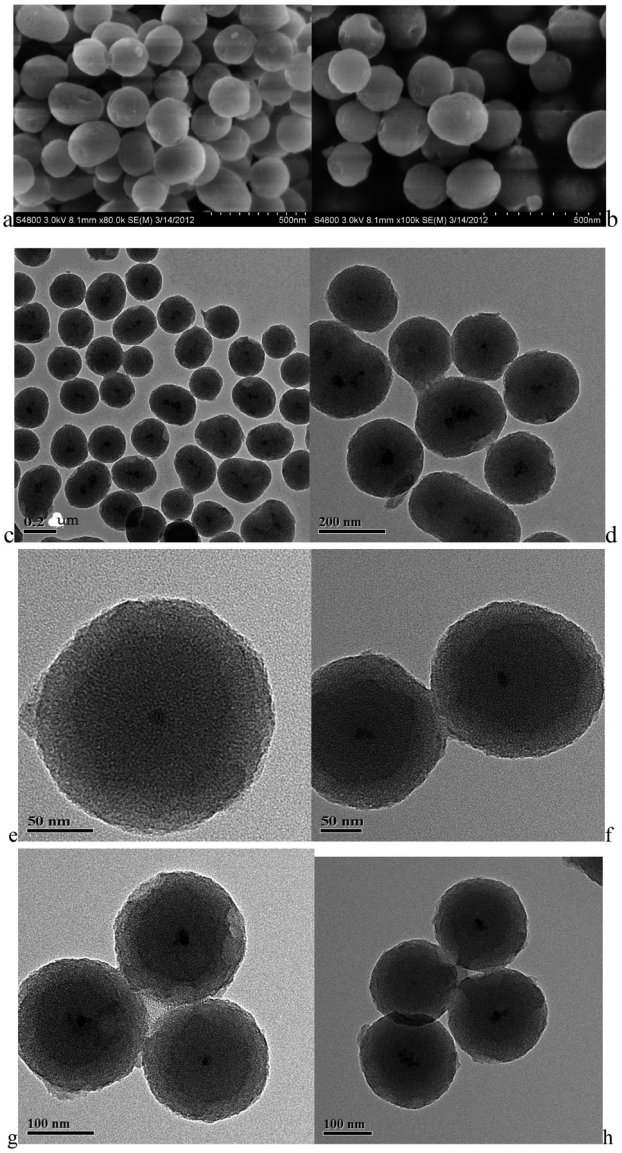

Fig. 5 SEM images of MMS (a) and Eu(ZnO-MMS)$(NTA)_3$ (b); and TEM images of Eu(ZnO-MMS)$(NTA)_3$ (c)–(h).

And the total size of the ZnO-containing magnetic mesoporous silica nanospheres is about 200 nm.

The magnetic properties of ZnO-MMS, Eu(ZnO-MMS)$(NTA)_3$ and Eu(ZnO-MMS)$(INTA)_3$ are recorded using vibration sample magnetometer at room temperature (see Fig. 6). The zero coercivity and the reversible hysteresis behavior indicate the magnetic silica spheres are superparamagnetic at room temperature. As shown in the figure, the saturation magnetization values of ZnO-MMS, Eu(ZnO-MMS)$(NTA)_3$ and Eu(ZnO-MMS)$(INTA)_3$ are 1.85, 0.94 and 0.72 emu per gram, respectively. And it can be inferred that the saturation magnetization value will increase with reducing the thickness of silica coating, which can be explained by the diamagnetic contribution of the thick silica shell surrounding the magnetic cores.[13b,17b] These nanocomposites with superparamagnetic

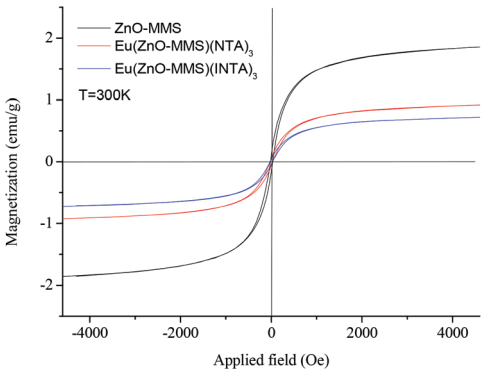

Fig. 6 Magnetization curves at 300 K of ZnO-MMS, Eu(ZnO-MMS)$(NTA)_3$ and Eu(ZnO-MMS)$(INTA)_3$.

characteristics can be used in biomedical applications because they can quickly react to an applied external magnetic field.

The luminescence performance of lanthanide hybrids has been investigated at room temperature. The excitation and emission spectra of the europium hybrid materials Eu(ZnO-MMS)$(L)_3$ (L = CNTA, NTA, INTA) are shown in Fig. 7(a) and (b), respectively. The excitation spectra of them are obtained by monitoring the emission of Eu^{3+} ion at 614 nm. A broad band ranging from 200 to 500 nm in the ultraviolet region can be observed from Fig. 7(a), which is attributed to the absorption of ZnO-MMS host and the Eu–O charge transfer

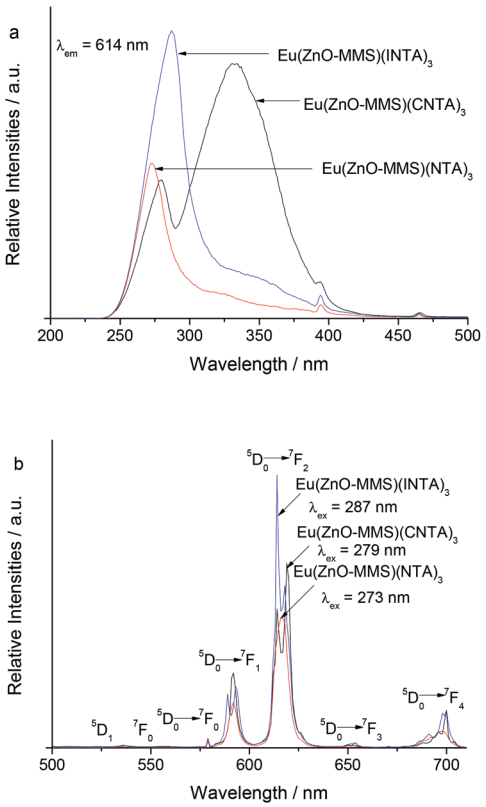

Fig. 7 The excitation (a) and emission (b) spectra of Eu(ZnO-MMS)$(L)_3$ (L = CNTA, NTA and INTA).

state (CTS, caused by interaction between the organic groups and the Eu^{3+} ion coordinated oxygen atoms). The two kinds of absorption are both overlapped. In their emission spectra, the strong red luminescence is obtained and five main emission peaks of Eu^{3+} are observed, which indicates the effective energy transfer takes place and conjugated systems form between organic ligands and Eu^{3+} ion. As we known, *via* the intramolecular energy transfer process, the sensitizers absorb energy and then transfer the energy to the accepting energy level of lanthanide ions relying on the energy gap between the triplet state energy of organic ligands and the resonance energy level of the central Ln^{3+} ions. The emission bands of three hybrid materials are assigned to the $^5D_0 \rightarrow {}^7F_J$ (J = 0–4) transitions at 579, 591, 615, 650, and 697 nm under excitation at 340, 270 and 270 nm, respectively. Among the transitions of the materials, the $^5D_0 \rightarrow {}^7F_2$ transition shows the strongest emission at about 614 nm. It is known that $^5D_0 \rightarrow {}^7F_1$ transition can be used as a reference to compare luminescent intensities of different Eu^{3+}-containing materials because $^5D_0 \rightarrow {}^7F_1$ transition does not depend on the chemical environments around the Eu^{3+}. It corresponds to a parity-allowed magnetic dipole transition. On the contrary, the $^5D_0 \rightarrow {}^7F_2$ transition is a typical electric dipole transition and strongly varies with the local symmetry of Eu^{3+}. The europium complexes will become more non-symmetrical and the intensity of the electric-dipolar transitions will become stronger when the micro-chemical environment offers stronger effects to Eu^{3+}. Usually the intensity ratio of $^5D_0 \rightarrow {}^7F_2$ (electric-dipolar transition) to $^5D_0 \rightarrow {}^7F_1$ (magnetic-dipolar transition), so-called red/orange ratio, has been widely used as an indicator of Eu^{3+} site symmetry.[23] Consequently the emission spectra show that the intensity ratios of the three curves in the three hybrid materials Eu(ZnO-MMS)$(L)_3$, L = CNTA, NTA and INTA are 4.66, 3.20 and 7.90, respectively. Therefore, it is proved that Eu^{3+} is situated in the similar local coordination environment for the same ZnO-MMS composite host and effective energy transfer has taken place between the organic groups and europium ions. In addition, there exists one weak emission peak at around 490 nm, which is corresponded to the emission of ZnO of ZnO-containing magnetic mesoporous silica nanomaterial. This indicates the luminescence of the substrate is quenched by Eu^{3+} as a result of the energy transfer between them and the hybrid system is effective for the luminescence of Eu^{3+}.

Fig. 8 shows the excitation (a) and emission (b) spectra of terbium hybrid materials Tb(ZnO-MMS)$(NTA)_3$ and Tb(ZnO-MMS)$(NTA)_3$. The excitation spectra are received by monitoring the emission of Tb^{3+} at 545 nm. The spectra are all dominated by a broad band from 200 to 450 nm and only an apparent excitation band appears in the short wavelength ultraviolet region centered at about 270 nm, which is ascribed to the ligand-to-metal charge transfer (LMCT) transition caused by interaction between organic groups and terbium ions. The intensity of the f–f absorption transition can not be observed obviously because it is much weaker than the absorption of host for being forbidden. The emission lines of the hybrid materials are assigned to the transitions from the

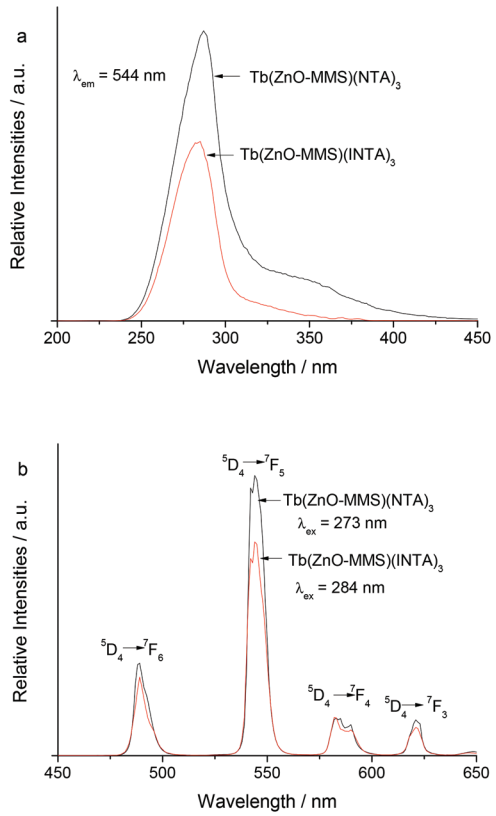

Fig. 8 The excitation (a) and emission (b) spectra of Tb(ZnO-MMS)$(L)_3$ (L = NTA and INTA).

$^5D_4 \rightarrow {}^7F_J$ (J = 6, 5, 4, 3) transitions at about 488, 544, 584 and 622 nm, respectively. And the $^5D_4 \rightarrow {}^7F_5$ transition shows the most striking green luminescence at about 544 nm, showing the organic ligands act as an efficient antenna for Tb^{3+}.

For further study of luminescence properties of the multi-component hybrids, the typical decay curves of them are measured at room temperature (see the data in Table 2). All of them can be described as a single exponential in the $\ln[S(t)/S_0] = -k_1 t = -t/\tau$, which shows that all lanthanide ions occupy the same average coordination environment. From Table 2, It can be seen that the resulting luminescent lifetimes of Eu^{3+}-containing hybrid materials increased in the order Eu(ZnO-MMS)-$(INTA)_3$ (0.43 ms) < Eu(ZnO-MMS)$(CNTA)_3$ (0.50 ms) < Eu-(ZnO-MMS)$(NTA)_3$ (0.80 ms). The luminescent lifetimes of Eu-(ZnO-MMS)$(CNTA)_3$ and Eu(ZnO-MMS)$(NTA)_3$ are similar, while the luminescent lifetime of Eu(ZnO-MMS)$(INTA)_3$ is relatively short. This result indicates that CNTA and NTA may play a more important role in protecting Eu^{3+} ion from quenching than INTA. For Tb^{3+}-containing hybrid materials, the lifetimes of Tb(ZnO-MMS)$(NTA)_3$ and Tb(ZnO-MMS)$(INTA)_3$ are 0.61 and 0.35 ms, which is shorter than those of corresponding Eu^{3+}-containing hybrid materials.

Table 2 Photoluminescent data of the resulting materials[a]

Hybrids	I_{02}/I_{01}	τ^a (ms)	$1/\tau$ (s^{-1})	A_r (s^{-1})	η (%)
Eu(ZnO-MMS)$(NTA)_3$	3.20	0.50	2000	260	10.2 (13.0)
Eu(ZnO-MMS)$(INTA)_3$	3.70	0.43	6250	280	7.4 (8.5)
Eu(ZnO-MMS)$(CNTA)_3$	4.66	0.80	2381	338	32.2 (14.2)
Tb(ZnO-MMS)$(NTA)_3$		0.61			68.5
Tb(ZnO-MMS)$(INTA)_3$		0.35			19.9

[a] The experiment data error for the data of luminescent intensity, lifetime and quantum yields are ±10%.

By means of the emission spectra of Eu^{3+} hybrids and the lifetimes of Eu^{3+} first excited level (τ, $^5D_0$), the emission quantum efficiency (η) of the $^5D_0$ excited state can be calculated. Assuming that only nonradiative and radiative processes are essentially involved in the depopulation of the $^5D_0$ excited state, η can be defined as follows:[24]

$$\eta = A_r/(A_r + A_{nr}) \quad (1)$$

here A_r and A_{nr} are radiative and nonradiative transition rates, respectively. A_r can be obtained by summing over the radiative rates A_{0J} for each $^5D_0 \rightarrow {}^7F_J$ (J = 0–4) transitions of Eu^{3+} as follows:

$$A_r = \Sigma A_{0J} = A_{00} + A_{01} + A_{02} + A_{03} + A_{04} \quad (2)$$

The branching ratio for the $^5D_0 \rightarrow {}^7F_{5,\ 6}$ transitions can be neglected, since both of them are not detected experimentally, and its influence can be ignored in the depopulation of the $^5D_0$ excited state. As $^5D_0 \rightarrow {}^7F_1$ transition belongs to the isolated magnetic dipole transition, it is nearly independent of the chemical environments around Eu^{3+} ion, and so can be regarded as an internal reference for the whole spectrum; the experimental coefficients of spontaneous emission, A_{0J}, can be calculated according to the relation:[25]

$$A_{0J} = A_{01}\ (I_{0J}/I_{01})\ (\nu_{01}/\nu_{0J}) \quad (3)$$

here, A_{0J} is the experimental coefficient of spontaneous emission. A_{01} is the Einstein coefficient of spontaneous emission between the $^5D_0$ and $^7F_1$ energy levels. A_{01} value is 14.65 s^{-1} in vacuum and can be determined to be about 50 s^{-1} in the air atmosphere.[26] I_{01} and I_{0J} are the integrated intensities of the $^5D_0 \rightarrow {}^7F_1$ and $^5D_0 \rightarrow {}^7F_J$ transitions (J = 0–4), respectively. Moreover, ν_{01} and ν_{0J} ($\nu_{0J} = 1/\lambda_J$) are the energy barycenters of the $^5D_0 \rightarrow {}^7F_1$ and $^5D_0 \rightarrow {}^7F_J$ transitions, respectively.

Nonradiative process influences the experimental luminescence lifetime by the following equation:

$$\tau_{exp} = (A_r + A_{nr})^{-1} \quad (4)$$

So quantum efficiency η can be calculated from radiative transition rate constant and experimental luminescence lifetime from the follow relation:

$$\eta = A_r \tau_{exp} \quad (5)$$

Based on the above discussion, it can be seen that the value of η largely depends upon the values of lifetimes and I_{02}/I_{01} ratio. The quantum efficiency will be high, if the lifetime and red/orange ratio are large. From Table 2, the quantum efficiencies of three kinds of Eu^{3+}-containing hybrid materials

follow this order Eu(ZnO-MMS)$(CNTA)_3$ > Eu(ZnO-MMS)$(NTA)_3$ > Eu(ZnO-MMS)$(INTA)_3$. The value η of Eu(ZnO-MMS)$(CNTA)_3$ and Eu(ZnO-MMS)$(CNTA)_3$ are close, but a big difference for Eu(ZnO-MMS)$(INTA)_3$. For the three kinds of hybrid materials, they have the same host of ZnO-MMS, and the only difference is the assistant ligand. The material of Eu(ZnO-MMS)$(CNTA)_3$ has largest I_{02}/I_{01} ratio and a longer lifetime, so its quantum efficiency are highest. Furthermore, the absolute quantum yields based on the integrating sphere for all the lanthanide hybrid systems are determined, which are higher than the calculated value. Especially Eu(ZnO-MMS)$(CNTA)_3$ and Tb(ZnO-MMS)$(NTA)_3$ possess high quantum yield values of 32.2% and 68.5%, respectively. So the different composition, energy match and coordination behavior will have influences on the luminescent performance of these multi-component hybrid materials.

Conclusion

We have designed and assembled lanthanide complexes functionalized magnetic mesoporous silica nanospheres covalently bonded with polymer modified ZnO unit. All the resulting hybrid materials have kept their spherical structure with mesoscopic ordering and wrapped in Fe_3O_4 nanoparticles. These multifunctional nanocomposites both have magnetic and luminescent properties by further introducing lanthanide complexes. Their photoluminescent behaviors are discussed deeply. The results may provide a strategy to connect two kinds of nanoparticles Fe_3O_4 and ZnO, along with lanthanide ions to mesoporous silica nanospheres to prepare multifunctional nanocomposites. Especially Eu(ZnO-MMS)$(CNTA)_3$ and Tb(ZnO-MMS)$(NTA)_3$ possess high quantum yield values of 32.2% and 68.5%, respectively. The functional integration of luminescence and magnetism will embody these kinds of multifunctional hybrids to have several advantages for potential applications, which will be explored the new applications in super-high intensity information storage, biological molecule recognition or imaging and drug delivery.

Acknowledgements

This work was supported by the National Natural Science Foundation of China (20971100, 91122003) and the Program for New Century Excellent Talents in University (NCET 2008-08-0398).

References

1 (*a*) Y. J. Li, B. Yan and Y. Li, *J. Solid State Chem.*, 2010, **183**, 871; (*b*) Y. J. Li and B. Yan, *Inorg. Chem.*, 2009, **48**, 8276; (*c*) K. Sheng, B. Yan, H. F. Lu and L. Guo, *Eur. J. Inorg. Chem.*, 2010, 3498; (*d*) L. Guo, B. Yan, K. Sheng and X. L. Wang, *Dalton Trans.*, 2011, **40**, 632; (*e*) Y. J. Li, B. Yan and Y. Li, *Chem.–Asian J.*, 2010, **5**, 1642.

2 (*a*) L. D. Carlos, R. A. S. Ferreira, V. D. Bermudez and S. J. L. Ribeiro, *Adv. Mater.*, 2009, **21**, 509; (*b*) K. Binnemans, *Chem. Rev.*, 2009, **109**, 4283; (*c*) B. Yan, *RSC Adv.*, 2012, **2**, 9304; (*d*) J. Feng and H. J. Zhang, *Chem. Soc. Rev.*, 2013, **42**, 387.

3 (*a*) X. G. Huang, Q. Wang, X. H. Yan, J. Xu, W. S. Liu, Q. Wang and Y. Tang, *J. Phys. Chem. C*, 2011, **115**, 2332; (*b*) X. F. Qiao and B. Yan, *J. Phys. Chem. B*, 2009, **113**, 11865.

4 (*a*) K. Binnemans and C. Gorller-Walrand, *Chem. Rev.*, 2002, **102**, 2303; (*b*) R. Van Deun, D. Moors, B. De Fre and K. Binnemans, *J. Mater. Chem.*, 2003, **13**, 1520.

5 (*a*) V. D. Z. Bermudez, R. A. S. Ferreira, L. D. Carlos, C. Molina, K. Dahmouche and S. J. L. Ribeiro, *J. Phys. Chem. B*, 2001, **105**, 3378; (*b*) S. Gago, J. A. Fernandes, J. P. Rainho, R. A. S. Ferreira, M. Pillinger, A. A. Valente, T. M. Santos, L. D. Carlos, P. J. A. Ribeiro-Claro and I. S. Goncalves, *Chem. Mater.*, 2005, **17**, 5077; (*c*) P. Liu, H. R. Li, Y. G. Wang, B. Y. Liu, W. J. Zhang, Y. J. Wang, W. D. Yan, H. J. Zhang and U. Schubert, *J. Mater. Chem.*, 2008, **18**, 735; (*d*) H. R. Li, P. Liu, Y. G. Wang, L. Zhang, J. B. Yu, H. J. Zhang, B. Y. Liu and U. Schubert, *J. Phys. Chem. C*, 2009, **113**, 3945.

6 (*a*) H. Weller, *Angew. Chem., Int. Ed. Engl.*, 1993, **32**, 41; (*b*) A. P. Alivisatos, *J. Phys. Chem.*, 1996, **100**, 13226.

7 (*a*) X. Michalet, F. F. Pinaud, L. A. Bentolila, J. M. Tsay, S. Doose, J. J. Li, G. Sundaresan, A. M. Wu, S. S. Gambhir and S. Weiss, *Science*, 2005, **307**, 538; (*b*) D. Gerion, F. Pinaud, S. C. Williams, W. J. Parak, D. Zanchet, S. Weiss and A. P. Alivisatos, *J. Phys. Chem. B*, 2001, **105**, 8861.

8 D. V. Talapin, A. L. Rogach, E. V. Shevchenko, A. Kornowski, M. Haase and H. Weller, *J. Am. Chem. Soc.*, 2002, **124**, 5782.

9 (*a*) M. Bruchez Jr., M. Moronne, P. Gin, S. Weiss and A. P. Alivisatos, *Science*, 1998, **281**, 2013; (*b*) T. Pellegrino, L. Manna, S. Kudera, T. Liedl, D. Koktysh, A. L. Rogach, S. Keller, J. Radler, G. Natile and W. J. Parak, *Nano Lett.*, 2004, **4**, 703; (*c*) F. Pinaud, D. King, H. P. Moore and S. Weiss, *J. Am. Chem. Soc.*, 2004, **126**, 6115; (*d*) S. Pathak, S. K. Choi, N. Arnheim and M. E. Thompson, *J. Am. Chem. Soc.*, 2001, **123**, 4103.

10 A. L. Rogach, L. Katsikas, A. Kornowsik, D. Su, A. Eychmüller and H. Weller, *Ber. Bunsen-Ges. Phys. Chem.*, 1996, **100**, 1772.

11 R. N. Bhargava, D. Gallagher, X. Hong and A. Nurmikko, *Phys. Rev. Lett.*, 1994, **72**, 416.

12 (*a*) J. Ugelstad, P. C. Mork, K. H. Kaggerud, T. Ellingsen and A. Berge, *Adv. Colloid Interface Sci.*, 1980, **13**, 101; (*b*) J. Ugelstad, A. Berge, T. Ellingsen, R. Schmid, T. N. Nilsen, P. C. Mork, P. Sienstad, E. Hornes and O. Olsvik, *Prog. Polym. Sci.*, 1992, **17**, 87.

13 (*a*) J. Halavaara, P. Tervahartiala, H. Isoniemi and K. Hockerstedt, *Acta Radiol.*, 2002, **43**, 180; (*b*) A. Y. Louie, M. M. Huber, E. T. Ahrens, U. Rothbacher, R. Moats, R. E. Jacobs, S. E. Fraser and T. J. Meade, *Nat. Biotechnol.*, 2000, **18**, 321; (*c*) A. S. Lubbe, C. Alexiou and

C. J. Bergemann, *J. Surg. Res.*, 2001, **95**, 200; (*d*) J. M. Perez, F. J. Simeone, A. Tsourkas, L. Josephson and R. Weissleder, *Nano Lett.*, 2004, **4**, 119.

14 (*a*) B. Y. Du, A. X. Mei, P. J. Tao, B. Zhao, Z. Cao, J. J. Nie, J. T. Xu and Z. Q. Fan, *J. Phys. Chem. C*, 2009, **113**, 10090; (*b*) H. Xu, L. L. Cui, N. H. Tong and H. C. Gu, *J. Am. Chem. Soc.*, 2006, **128**, 15582.

15 X. F. Qiao, H. Y. Zhang and B. Yan, *Dalton Trans.*, 2010, **39**, 8882.

16 (*a*) V. Salgueiriño-Maceira, M. A. Correa-Duarte, M. Spasova, L. M. Liz-Marzán and M. Farle, *Adv. Funct. Mater.*, 2006, **16**, 509; (*b*) Y. F. Shao, B. Yan and Q. P. Li, *Eur. J. Inorg. Chem.*, 2013, 9192.

17 (*a*) H. M. Xiong, Z. D. Wang, D. P. Liu, J. S. Chen, Y. G. Wang and Y. Y. Xia, *Adv. Funct. Mater.*, 2005, **15**, 1751; (*b*) H. M. Xiong, Z. D. Wang and Y. Y. Xia, *Adv. Mater.*, 2006, **18**, 748; (*c*) H. M. Xiong, X. Zhao and J. S. Chen, *J. Phys. Chem. B*, 2001, **105**, 10169; (*d*) Y. F. Shao and B. Yan, *Dalton Trans.*, 2012, **41**, 7423; (*e*) Y. F. Shao, B. Yan and Z. Y. Jiang, *RSC Adv.*, 2012, **2**, 9192.

18 (*a*) S. Y. Yu, H. J. Zhang, J. B. Yu, C. Wang, L. N. Sun and W. D. Shi, *Langmuir*, 2007, **23**, 7836; (*b*) W. Q. Fan, J. Feng, S. Y. Song, Y. Q. Lei, Y. Xing, R. P. Deng, S. Dang and H. J. Zhang, *Eur. J. Inorg. Chem.*, 2008, 5513; (*c*) J. Feng, S. Y. Song, R. P. Deng, W. Q. Fan and H. J. Zhang, *Langmuir*, 2010, **26**, 3596; (*d*) Y. F. Shao, B. Yan and Q. P. Li, *Eur. J. Inorg. Chem.*, 2013, 381.

19 M. V. Landau, S. P. Varkey, M. Herskowitz, O. Regev, S. Pevzner, T. Sen and Z. Luz, *Microporous Mesoporous Mater.*, 1999, **33**, 149.

20 D. L. Dexter, *J. Chem. Phys.*, 1953, **21**, 836.

21 C. T. Kresge, M. E. Leonowicz, W. J. Roth, J. C. Vartuli and J. S. Beck, *Nature*, 1992, **359**, 710.

22 (*a*) D. H. Everett, *Pure Appl. Chem.*, 1972, **31**, 577; (*b*) W. H. Zhang, X. B. Lu, J. H. Xi, Z. L. Hua, L. X. Zhang, M. Robertson, J. L. Shi, D. S. Yan and J. D. Holmes, *Adv. Funct. Mater.*, 2004, **14**, 544.

23 K. S. Guan and Y. S. Yin, *Mater. Chem. Phys.*, 2005, **92**, 10.

24 P. C. R. Soares-Santos, H. I. S. Nogueira, V. Félix, M. G. B. Drew, R. A. S. Ferreira, L. D. Carlos and T. Trindade, *Chem. Mater.*, 2003, **15**, 100.

25 (*a*) E. E. S. Teotonio, J. G. P. Espinola, H. F. Brito, O. L. Malta, S. F. Oliveria, D. L. A. de Foria and C. M. S. Izumi, *Polyhedron*, 2002, **21**, 1837; (*b*) M. F. Hazenkamp and G. Blasse, *Chem. Mater.*, 1990, **2**, 105.

26 M. H. V. Werts, R. T. F. Jukes and J. W. Verhoeven, *Phys. Chem. Chem. Phys.*, 2002, **4**, 1542.